

Water-Mediated Charge Transfer and Electron Localization in a Co_3Fe_2 Cyanide-Bridged Trigonal Bipyramidal Complex

Emily Hruska, Quansong Zhu, Somnath Biswas, Matthew T. Fortunato, Dustin R. Broderick, Christine M. Morales, John M. Herbert, Claudia Turro, and L. Robert Baker*



Cite This: *J. Am. Chem. Soc.* 2024, 146, 8031–8042



Read Online

ACCESS |



Metrics & More

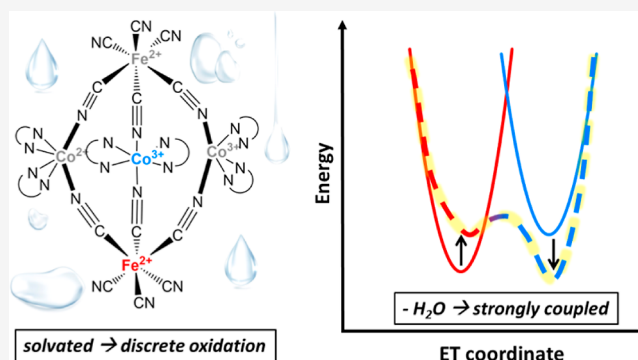


Article Recommendations



Supporting Information

ABSTRACT: The effects of temperature and chemical environment on a pentanuclear cyanide-bridged, trigonal bipyramidal molecular paramagnet have been investigated. Using element- and oxidation state-specific near-ambient pressure X-ray photoemission spectroscopy (NAP-XPS) to probe charge transfer and second order, nonlinear vibrational spectroscopy, which is sensitive to symmetry changes based on charge (de)localization coupled with DFT, a detailed picture of environmental effects on charge-transfer-induced spin transitions is presented. The molecular cluster, $\text{Co}_3\text{Fe}_2(\text{tmphen})_6(\mu\text{-CN})_6(\text{t-CN})_6$, abbrev. Co_3Fe_2 , shows changes in electronic behavior depending on the chemical environment. NAP-XPS shows that temperature changes induce a metal-to-metal charge transfer (MMCT) in Co_3Fe_2 between a Co and Fe center, while cycling between ultrahigh vacuum and 2 mbar of water at constant temperature causes oxidation state changes not fully captured by the MMCT picture. Sum frequency generation vibrational spectroscopy (SFG-VS) probes the role of the cyanide ligand, which controls the electron (de)localization via the superexchange coupling. Spectral shifts and intensity changes indicate a change from a charge delocalized, Robin-Day class II/III high spin state to a charge-localized, class I low spin state consistent with DFT. In the presence of a H-bonding solvent, the complex adopts a localized electronic structure, while removal of the solvent delocalizes the charges and drives an MMCT. This change in Robin-Day classification of the complex as a function of chemical environment results in reversible switching of the dipole moment, analogous to molecular multiferroics. These results illustrate the important role of the chemical environment and solvation on underlying charge and spin transitions in this and related complexes.



INTRODUCTION

Understanding the nature of spin dynamics in molecules is critical for realizing the potential applications of molecular switches, which range from molecular design of information storage systems¹ to quantum information processing^{2–4} and quantum sensing^{1,5} to photochemistry^{6,7} and photocatalysis.^{8,9} Each of these applications can benefit from the ability to control the local charge and spin configurations in multimetallic systems. In both solid state systems and molecular complexes, this capability is often derived from bistability, which enables switching between various stable or metastable charge and spin configurations based on external stimuli. For example, the discovery of Prussian blue (PB) analogues and their extended magnetic ordering at elevated temperatures has led to a high interest in understanding cyanide chemistry for magnetic applications.^{10–14} Translating the PB groundwork to molecular complexes of varied geometries has paved the way for studies in many interesting mechanistic behaviors, including single molecule magnetism,¹⁵ cyanide linkage isomerism,^{16,17} charge transfer induced spin transitions

(CTIST),^{18–23} and light induced excited spin state trapping (LIESST).^{24–26}

Synthetic protocols for the design of multimetallic complexes have enabled a range of structural motifs to be studied in the search for bistable molecular magnets. While examples exist of organic^{27–30} and lanthanide-based molecular magnets,^{31–36} low-cost, earth-abundant transition metal complexes represent an attractive and widely studied platform for designing molecular bistability based on electron spin.^{35,37–41}

Bimetallic systems consisting of d^4 through d^7 transition metals often display spin transitions that are coupled to electron exchange between metal centers. Such spin crossover

Received: October 15, 2023

Revised: February 28, 2024

Accepted: February 29, 2024

Published: March 13, 2024



events may be triggered by various external stimuli, including temperature, light, or chemical environment; however, achieving molecular bistability at room temperature remains a challenge. A number of recent studies have shown that high nuclearity clusters with intentional ligand motifs can provide bistable spin configurations with high ground state magnetic susceptibility.^{36,42–44}

While synthetic tunability of the ligand framework enables preparation of a variety of model complexes, a lack of direct measurements of element specific oxidation state and charge (de)localization limits current mechanistic understanding that could otherwise inform the rational design of functional molecular systems. The Robin-Day classification system categorizes mixed valence systems by the strength of the electronic coupling between metal centers.^{45–47} In multi-metallic complexes based on cyanide bridging ligands, the strength of superexchange coupling ultimately defines the degree of localization of valence electrons in the system. In this study, we focus on a pentanuclear cluster $\text{Co}_3\text{Fe}_2(\text{tmphen})_6(\mu\text{-CN})_6(t\text{-CN})_6$ (tmphen = 3,4,7,8-tetramethyl-1,10-phenanthroline) with bridging and terminal cyanide ligands, $\mu\text{-CN}$ and $t\text{-CN}$, respectively, abbreviated Co_3Fe_2 .

This complex has been reported to display electronic and magnetic bistability, which can be switched using both temperature and visible light.^{18,48,49} However, it has also been reported that both the optical properties and magnetic susceptibility are sensitive to the chemical environment, where exposure to moisture induces a color change as well as a significant reduction in the magnetic susceptibility at a fixed temperature.^{48,49} Using a combination of near-ambient pressure X-ray photoemission spectroscopy (NAP-XPS), Raman spectroscopy, sum frequency generation vibrational spectroscopy (SFG-VS), and DFT calculations, we investigate the effect of the chemical environment on the local oxidation states of both Co and Fe centers as well as the degree of electron (de)localization based on the effect of solvation on the superexchange coupling in this complex. We determine that the Robin-Day classification of the complex plays an important role in the mechanism of electronic and magnetic bistability. We also show that switching between a class I and a class II/III system involves large changes in the dipole moment of the molecule, extending the properties that can be reversibly switched in this bistable system. This work highlights the critical role of molecular solvation on the electronic and magnetic properties of this and related systems and shows that mechanistic understanding of external switching depends strongly on the strength of electronic superexchange, which varies significantly as a function of the chemical environment.

EXPERIMENTAL SECTION

Synthesis. The synthetic protocol of the Co_3Fe_2 complex has been previously investigated and reported by Dunbar et al.^{17,48,49} and is detailed in the Supporting Information. In short, a hydrous cobalt nitrate was dissolved in acetonitrile and treated with the coordinating ligand, tetramethyl-1,10-phenanthroline. An iron salt dissolved in acetonitrile was slowly added to the solution. After filtration and 2 days wait time, a red anhydrous crystal was collected. Filtration in a humid atmosphere produced the blue solid form, which was used for all further experiments. Extensive characterization of the complex after synthesis is provided in the Supporting Information.

Sample Preparation. Spectroscopic samples were prepared by drop-casting a saturated solution of the blue solid form on ozone-cleaned Au substrates. The Au substrates were prepared by depositing a Au thin film layer on a Si or CaF_2 substrate using electron beam

evaporation (Denton DV-502A E-Gun Evaporator). They were further cleaned in an ozone cleaner for 30 min to remove any potential contaminants on the surface before drop-casting the Co_3Fe_2 solution. SFG-VS samples had a measured volume of 10 μL drop-casted on the substrate to produce consistent signal intensity, while the shallow probe depth of NAP-XPS measurements allowed for a thicker layer to give reproducible results.

X-ray Photoemission Spectroscopy. High resolution XPS analysis was performed using a Kratos Axis Ultra X-ray photoelectron spectrometer with a monochromatic Al $K\alpha$ X-ray source and a photon energy of 1486.6 eV. These measurements were performed at room temperature. Using the Casa XPS software, Fe 2p, Co 2p, and C 1s windows were fit with a Shirley background and a Gaussian–Lorentzian line shape of a 70:30 ratio. All spectra were calibrated to the adventitious C feature at 284.5 eV. Further details of the parameters used for the fitting are included in Supporting Information Section 2.

Near-Ambient Pressure X-ray Photoemission Spectroscopy. NAP-XPS was performed using a SPECS NAP-XPS system in the Surface Analysis Facility at Ohio State University. The system is equipped with a NAP-reaction cell where 0.5 and 2 mbar of a given solvent in the gas phase was introduced via a vial on the instrument manifold following freeze pump cycles to purify at room temperature. Temperature-dependent experiments were performed at sweeping points between 150 and 375 K in vacuum conditions.

Raman Microscopy. Raman spectra were acquired using a Renishaw InVia Microscope. The excitation wavelength is 785 nm. The sample is held in the same cell used in the SFG measurements at room temperature. The beam is focused on the front side of the sample using a Nikon (10 \times /0.30 NA, 17.5 mm working distance) objective and has a diameter of 2 μm . The power of the excitation beam at the sample is about 50 mW. During the measurement, direct Ar flow or water vapor flow purged by Ar was introduced into the cell, and the corresponding Raman spectra were collected three times with 60 s integration time for each. Three spectra were averaged and the background spectrum obtained from bare Au in each condition were subtracted to obtain the final spectra.

Vibrational Sum Frequency Generation Spectroscopy. SFG spectra were measured through a homemade cell using frontside geometry. The laser instrument setup has been described previously.^{50,51} In short, the Ti/sapphire regenerative amplifier (Spectra Physics-Solstice) outputs 90 fs pulses at 800 nm with a repetition rate of 2 kHz. 70% of the output is used to pump an optical parametric amplifier (Topas Prime), which generates the IR beam with a tunable wavelength and a spot size of 0.032 mm^2 . The remaining 30% visible beam is spectrally narrowed to about 10 cm^{-1} using an air-gap etalon (TecOptics) and focused to a spot size of 0.128 mm^2 . The incident angle for beams in the sample is 47°. The IR beam is centered at about 2100 cm^{-1} and has an energy of 3 μJ , while the visible beam has an energy of 10 μJ . Each spectrum was collected by delaying the visible beam relative to the IR beam by about 850 fs (Supporting Information) with an integration time of 2 min. To mirror the isolated vacuum chamber system of the NAP-XPS measurements, the beams go through a CaF_2 window and a gas gap before they reach the drop-cast Co_3Fe_2 sample on the Au substrate, where the sum frequency signal is generated in an isolated homemade cell at room temperature. A continuous Ar (>99.998%, Praxair) gas flow purging through the cell at a rate of 616 sccm was maintained throughout the measurement for vacuum-like conditions. For measurements in solvated chemical environments, the Ar gas flow went through a gas-tight vial first, which contained ultrapure water or methanol, and carried the evaporated chemicals into the cell.

Electronic Structure Calculations. Density functional theory (DFT) calculations were performed starting from the crystal structure in ref 49, which was then relaxed at the B(35)LYP+D3/def2-SV(P) level. The B(35)LYP exchange–correlation (xc) functional, defined as

$$E_{xc}^{\text{B(35)LYP}} = 0.65 E_x^{\text{B88}} + 0.35 E_x^{\text{HF}} + E_c^{\text{LYP}}$$

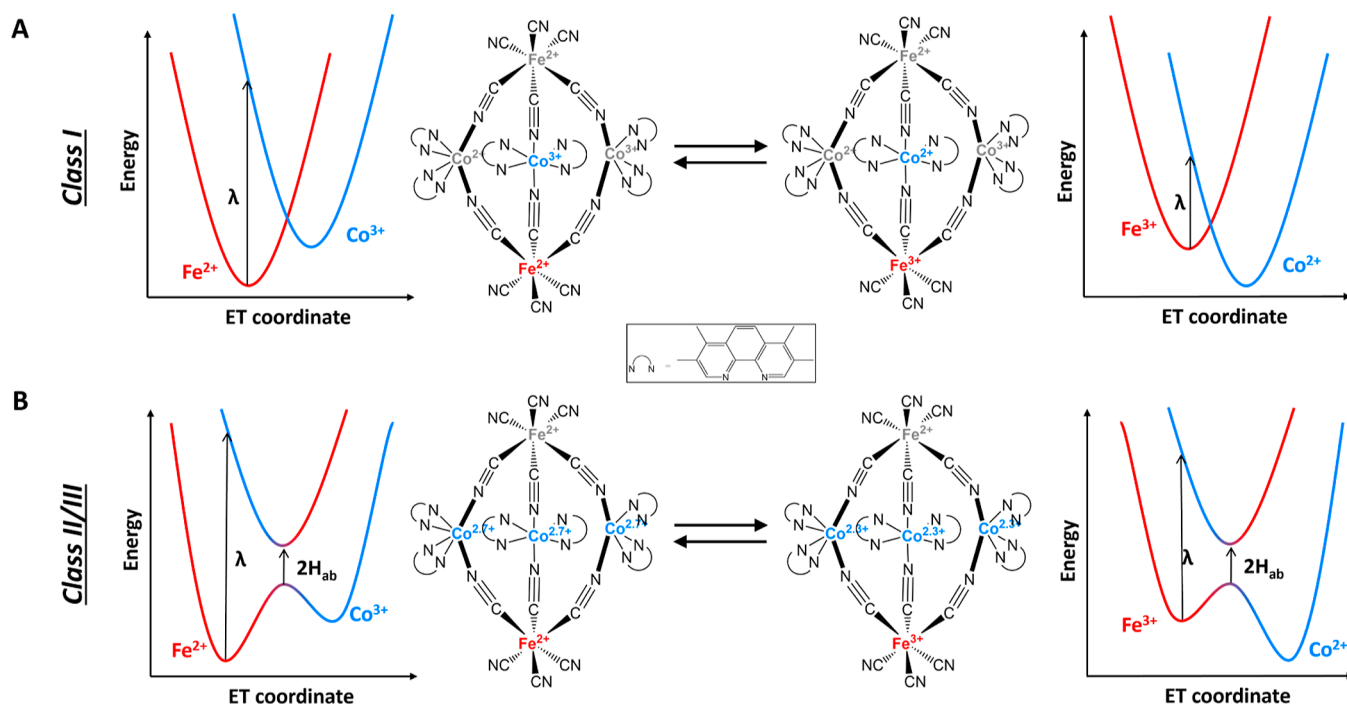


Figure 1. (A) Co_3Fe_2 (middle) with one Fe (red) and one Co (blue) involved in a reversible MMCT. The electron transfer versus energy plots to the left and right of each structure depict the stabilization of an electron on either Fe or Co centers under the class I localized charge picture. (B) Co_3Fe_2 (middle) with one Fe (red) and three Co (blue) involved in a reversible MMCT. The electron transfer versus energy plots to the left and right of each structure depict the shared delocalization of an electron on Fe and Co centers under the class II/III delocalized charge picture.

is one that is recommended for systems at the class II/III borderline,^{47,52} and is combined here with an empirical dispersion correction.⁵³ These calculations were performed using a broken-symmetry DFT approach⁵⁴ and are intended to elucidate energy differences between various spin and oxidation states. All calculations were performed using Q-Chem v. 6.1.⁵⁵

RESULTS AND DISCUSSION

Figure 1A shows the nominal process for electron transfer in a Co_3Fe_2 system assuming Robin-Day class I,⁴⁷ where the system has weak coupling between metal centers. In this picture, electron transfer is characterized by electron localization to discrete metal centers such that each metal exists in a well-defined oxidation state. This case is depicted in Figure 1A, where charge transfer occurs between an Fe center and a single Co center (shown in blue), with two Co centers acting as spectators (shown in gray). Alternatively, Figure 1B shows the analogous process for the case where the Co_3Fe_2 complex is categorized as a class II/III system with a small barrier for interconversion. Systems in class II/III may exhibit solvent- or conformation-driven switching between localized oxidation states.⁴⁶ Assuming strong coupling of the axial Fe centers to each of the equatorial Co centers through the bridging cyano ligands, as suggested by electronic structure calculations that are described below, we can see that electronic superexchange allows delocalization of electrons across multiple metal centers. In this scenario, it may become difficult to identify a single Co center involved in the charge transfer as electronic exchange between Fe and its three nearest neighboring Co centers becomes facile. This is depicted in Figure 1B as participation of all three equatorial Co centers (shown in blue) in the charge transfer event, making for a fully delocalized class II/III system with respect to the Co sites.

A measurement that samples the system on a time scale slower than the electronic exchange rate will observe an average oxidation state based on electron sharing between nearly equivalent Co centers rather than three distinct sites. As such, the distinction between class II, class II/III, and class III may depend on the time scale of the spectroscopic technique that is used,⁴⁷ and class II/III systems may exhibit characteristics of both localized and delocalized valence electrons.⁴⁶ Additionally, the molecular symmetry increases, and the dipole moment in the equatorial plane becomes negligible because of the strong coupling of the Co centers across the bridging cyanide ligands. In either case 1A or 1B, a metal-to-metal charge transfer (MMCT) event can be triggered depending on the environment of the molecule (temperature, solvent, etc.). However, given the two possibilities for charge dynamics, it becomes necessary to probe the metal centers locally to gain a better understanding of the nature of the charge transfer and associated spin transition based on the strength of electronic coupling in the system.

Electronic Structure Calculations. Broken-symmetry DFT calculations were used to investigate model spin/oxidation states. These calculations start from an initial guess having integer oxidation states on each metal site, from which we attempt to find an orbital-optimized solution to the Kohn–Sham equations that resembles the initial guess (this procedure has sometimes been called the “generalized ionic fragment” approach⁵⁶). Possible spin and oxidation states for the metal ions are depicted in Scheme 1. Note that the broken-symmetry Kohn–Sham solution is necessarily spin-contaminated, but such calculations can provide information regarding whether intervalence charge transfer, and thus charge delocalization, is energetically feasible. To do so, one must examine spin densities on the metal sites for various broken-symmetry solutions.

Scheme 1. Possible Spin States for Individual Metal Ions

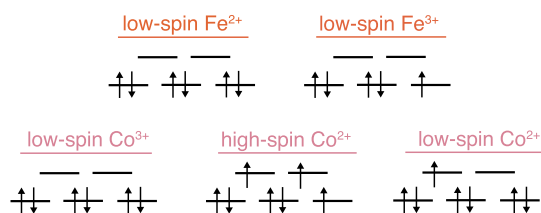


Figure 2A shows the spin density at the DFT-optimized geometry of a low-spin state with the configuration $(\text{Co}^{2+})-(\text{Co}^{3+})_2(\text{Fe}^{2+})_2$

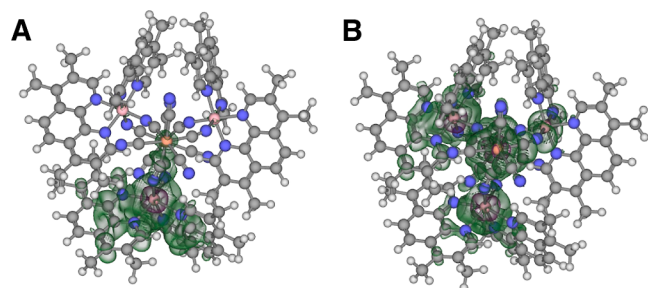


Figure 2. Spin densities ($\rho_\alpha - \rho_\beta$) for Co_3Fe_2 in (A) $(\text{Co}^{2+})-(\text{Co}^{3+})_2(\text{Fe}^{2+})_2$ state with $S = 3/2$ and (B) $(\text{Co}^{2+})_2(\text{Co}^{3+})(\text{Fe}^{2+})(\text{Fe}^{3+})$ state with $S = 7/2$. In both cases, the geometry is that optimized geometry for the $S = 3/2$ state. Both isosurfaces contain 90% of the spin density and are plotted looking down the Fe–Fe axis at the center. The Co_1 site, which maintains high-spin Co(II) character, is located at the bottom.

$(\text{Co}^{3+})_2(\text{Fe}^{2+})_2$, consisting of a single Co(II) ion in a high-spin configuration and low-spin configurations on the remaining metal centers, for a total spin of $S = 3/2$ (see Scheme 1). Crystallographic data demonstrate that the temperature-dependent magnetic properties of Co_3Fe_2 are associated with changes in oxidation state at the Co_2 and Co_3 sites, whereas Co_1 (located at the bottom in Figure 2) remains high-spin Co(II).^{18,49} In accord with the crystal structure that was used as a starting point, we obtain Co–N bond lengths that are ~ 0.2 Å longer at the Co_1 site as compared to Co_2 or Co_3 , characteristic of a class I or class II system.^{45,47} However, this could also be consistent with a class II/III system, specifically with readily switchable spin states based on small fluctuations in geometry, which are not sampled in these static calculations. Despite concerns that vacuum-exposed anionic moieties (such as CN^-) can cause DFT convergence problems,^{57,58} or that vacuum boundary conditions exaggerate charge delocalization (tending toward class III),⁴⁷ we obtain similar geometries when using a polarizable continuum model^{59–61} to add low-dielectric boundary conditions.

Figure 2B shows the spin density for a higher-spin $S = 7/2$ configuration, representing the configuration $(\text{Co}^{2+})_2(\text{Co}^{3+})(\text{Fe}^{2+})(\text{Fe}^{3+})$. In this particular model, Co_1 and Co_2 are both high-spin Co(II) while one of the Fe atoms has been oxidized to Fe(III) in order to maintain charge neutrality, and in Figure 2, the spin density for this $S = 7/2$ state is computed at the geometry that was optimized for the $S = 3/2$ state. According to calculations at the B(35)LYP+D3/def2-SV(P) level, the $S = 7/2$ configuration is 7 kcal/mol higher in energy than the $S = 3/2$ configuration at the geometry of the latter, although this energy difference is sensitive to the fraction of Hartree–Fock exchange; we regard this 7 kcal/mol difference as immaterial.

Spin contamination in these calculations is not severe, with $\langle \hat{S}^2 \rangle = 3.76$ and $16.01 \hbar^2$ for the low- and high-spin states, respectively, as compared to spin-pure theoretical values of 3.75 and $15.75 \hbar^2$.

We conclude that broken-symmetry DFT calculations are consistent with both states having nearly the same energy. These calculations say nothing about the barrier to interconversion but are not inconsistent with a switchable class II/III system where delocalization among the Co centers is mediated by the cyano ligands. Although Dunbar and co-workers consider a statistical mixture of high-spin Co(II) and low-spin Co(III) to be a more likely scenario as compared to charge delocalization, due to the absence of an orbital pathway between the Co ions,⁴⁹ spin densities in Figure 2 indicate spin polarization on the cyano ligands. This may provide a pathway for $\text{Co} \rightarrow \text{Co}$ MMCT that is mediated by Fe.

Attempts to optimize the geometry of the $S = 7/2$ state with the configuration $(\text{Co}^{2+})_2(\text{Co}^{3+})(\text{Fe}^{2+})(\text{Fe}^{3+})$ were unsuccessful, inevitably collapsing to $(\text{Co}^{2+})_3(\text{Fe}^{3+})_2$ with two high-spin Co(II) ions, one low-spin Co(II), and two Fe(III) ions with opposite spins. This form, which is observed by Dunbar and co-workers when the material is dried at high temperature under inert conditions,^{48,49} appears to be much lower in energy. Specifically, a $S = 9/2$ state corresponding to $(\text{Co}^{2+})_3(\text{Fe}^{3+})_2$ with all-parallel unpaired spins is 10 kcal/mol more stable than the $S = 3/2$ state at the optimized geometry of the latter and 132 kcal/mol more stable at its own optimized geometry.

Temperature-Dependent XPS. Figure 3 shows the XPS spectra of Co_3Fe_2 at temperatures ranging from 150 to 375 K. Fitting these spectra provides the oxidation state distribution of the two Fe and three Co metal centers as a function of the temperature. Figure 3A shows the Fe and Co 2p regions for the three representative temperatures. At 150 K, the Fe 2p core level shows 88.1% Fe^{2+} and 11.9% Fe^{3+} , while the Co 2p core level shows 44.6% Co^{2+} and 55.4% Co^{3+} . By increasing the temperature to 298 K, the Fe^{3+} contribution increases to 35.6% as the Fe oxidizes, and the Co^{2+} contribution increases to 53.1% as the Co reduces. By 375 K the contribution of oxidized Fe^{3+} increased to 49.7%, and the contribution of reduced Co^{2+} increased to 60.6%. Quantification of Fe and Co oxidation state ratios for the complete temperature series is shown in Figure 3B. These data are consistent with a near unity electron transfer from Fe to Co. From these results, it is clear that a one-electron MMCT occurs between the Fe and Co sites as a function of temperature. This reflects a temperature-driven switch from a primarily $(\text{Co}^{2+})-(\text{Co}^{3+})_2(\text{Fe}^{2+})_2$ state to a primarily $(\text{Co}^{2+})_2(\text{Co}^{3+})(\text{Fe}^{2+})(\text{Fe}^{3+})$ state. This matches the expected transition from a room-temperature, humid atmosphere-exposed $(\text{Co}^{2+})-(\text{Co}^{3+})_2(\text{Fe}^{2+})_2$ to a metastable $(\text{Co}^{2+})_2(\text{Co}^{3+})(\text{Fe}^{2+})(\text{Fe}^{3+})$ reported previously under dry conditions.⁴⁹ However, assuming a strongly coupled system (class II/III), this same MMCT could be equally well-described as a switch from $(\text{Co}^{2+})_3(\text{Fe}^{2+})_2$ to $(\text{Co}^{2+})_2(\text{Fe}^{2+})(\text{Fe}^{3+})$, where strong Fe–CN–Co coupling makes individual Co centers indistinguishable.

In either case, it is possible to define the effective electron balance during this MMCT process as

$$\text{Electron balance} = (2A_{\text{Fe}^{2+}} + 3A_{\text{Co}^{2+}})/3$$

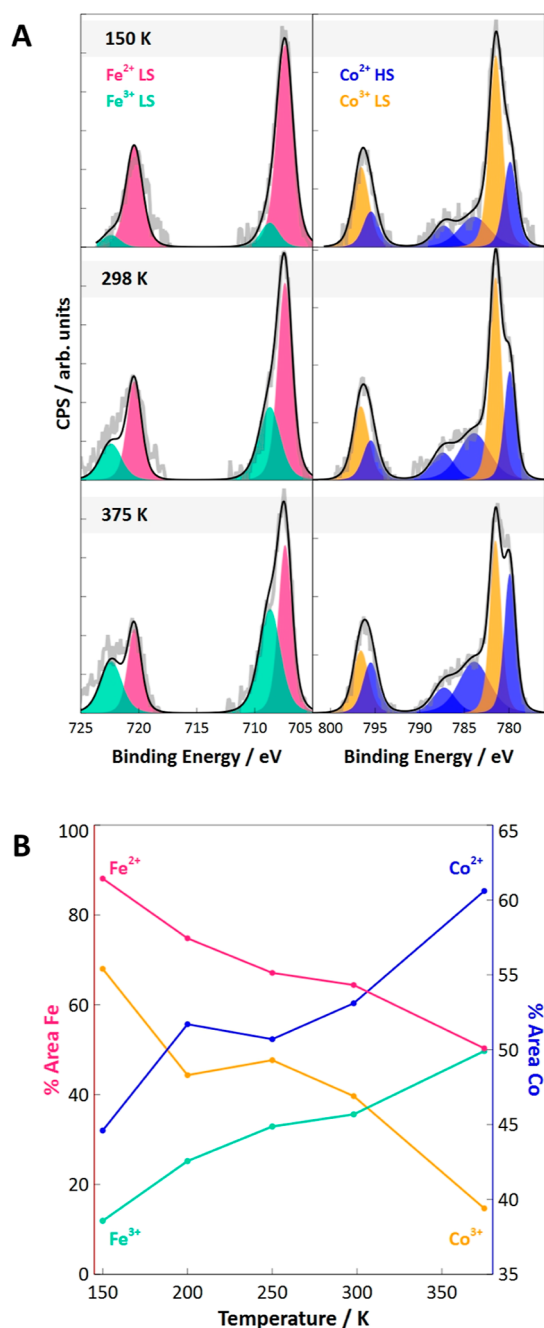


Figure 3. (A) NAP-XPS results at 150, 298, and 375 K of the Fe 2p (left) and Co 2p (right) core levels. Total background-subtracted counts are shown as the gray solid line. The total fit is shown as the black solid line. Individual components are highlighted in pink (Fe²⁺), green (Fe³⁺), blue (Co²⁺), and orange (Co³⁺). (B) Fe and Co % area from NAP-XPS spectral fits as a function of temperature. Each solid line represents a different oxidation state, where Fe²⁺ is in pink, Fe³⁺ is in green, Co²⁺ is in blue, and Co³⁺ is in orange.

where A is the area for the Fe and Co centers extracted from the XPS fits and weighted with the quantity of metal centers to reach a normalized value. This equation is derived from the concept that any neutral state of the molecule in its localized form would have 3 total metal centers with a 2+ charge. As expected, the electron balance remains close to unity for all XPS spectra measured between 150 and 375 K, consistent with a temperature-induced MMCT process. This is shown in Figure 4.

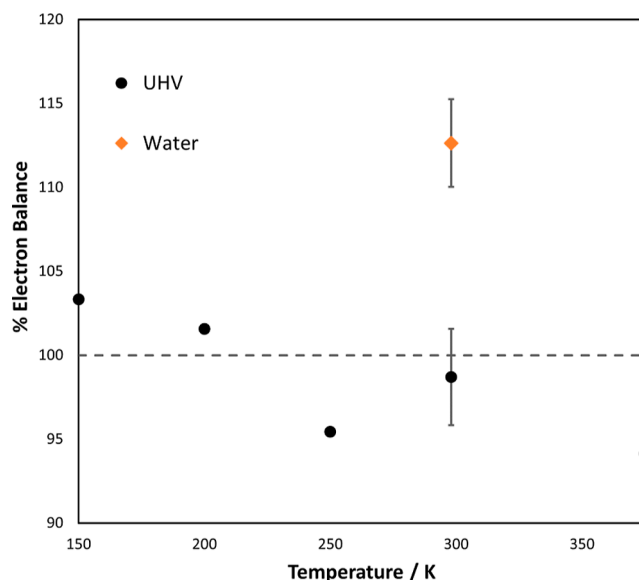


Figure 4. % Electron balance calculated for charge transfers at each temperature under vacuum (black circles) and with water exposure at room temperature (orange diamond). A dashed line at 100% is shown for reference to a unity MMCT. The uncertainty bars for the UHV and water values at 298 K represent the standard error calculated from multiple independent measurements on different samples.

Chemical Environment-Dependent XPS. While temperature-dependent XPS spectra are consistent with an MMCT switching mechanism, Figure 5 shows the effect of chemical environment-induced state switching measured with NAP-XPS for the Fe and Co 2p spectra under ultrahigh vacuum (UHV) and 2 mbar water vapor held at room temperature. Although 2 mbar is well below atmosphere, many NAP-XPS studies have used similar conditions to obtain important insights about behaviors under high pressure conditions.⁶² Further, while the chemical potential of water is lower at 2 mbar than at ambient pressure, it is much closer to ambient than to UHV,⁶³ where most XPS studies are performed, and the insight gained under these model conditions has consistently provided important and relevant insights for systems under actual application conditions.^{63–65}

In this series, the same sample was cycled from UHV to water vapor and pumped again to UHV to evaluate the reversibility of the switching process induced by the interaction with water vapor. When initially exposed to a UHV environment, the Fe 2p XPS spectrum appears as expected with both Fe²⁺ and Fe³⁺ present. The Co 2p spectrum shows a distribution of Co²⁺ and Co³⁺ character in approximately a 2:1 ratio. Introducing water into the system results in a reduction of Fe³⁺ to Fe²⁺. Surprisingly, the Co 2p spectrum shows slight oxidation of the Co, but this change is less than expected for a unity electron transfer from Co to Fe. When the water vapor is pumped out and UHV conditions are reestablished, the process reverses. This is observed in the Fe 2p spectrum as the single Fe²⁺ splits back into a near-equal contribution of Fe^{2+/3+}. Again, the Co 2p spectrum also reverses, but the change is less than expected for full electron transfer between Fe and Co. These findings highlight an important difference between temperature and chemical environment-induced switching in this complex. Comparing the electron balance for temperature-dependent spectra with multiple spectra measured in UHV and 2 mbar water at 298 K shows that upon exposure to water

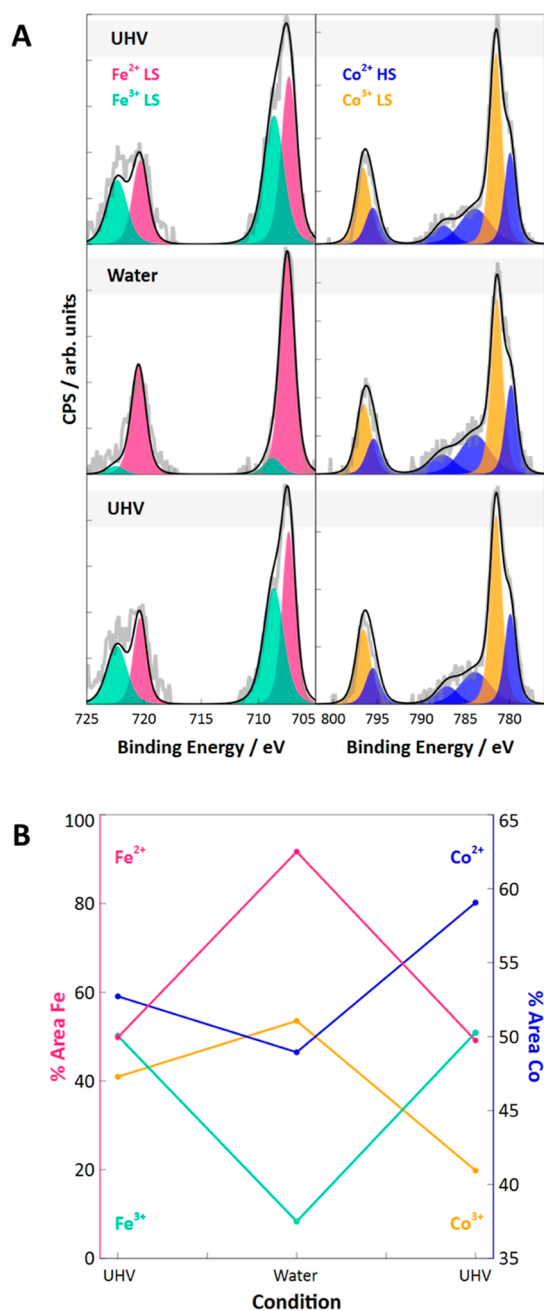


Figure 5. (A) NAP-XPS results at UHV, water, and post-exposure UHV of the Fe 2p (left) and Co 2p (right) core levels. Total background-subtracted counts are shown as the gray solid line. The total fit is shown as the black solid line. Individual components are highlighted in pink (Fe²⁺), green (Fe³⁺), blue (Co²⁺), and orange (Co³⁺). (B) Fe and Co % area from NAP-XPS spectral fits as a function of chemical environment. Each solid line represents a different oxidation state, where Fe²⁺ is in pink, Fe³⁺ is in green, Co²⁺ is in blue, and Co³⁺ is in orange.

vapor, the electron balance exceeds unity with statistical significance as shown in Figure 4.

We now consider multiple potential mechanisms to explain this surprising behavior. First, it is possible that exposure of the sample surface to X-ray radiation during XPS measurements can induce beam damage that mistakenly appears as a change in the chemical state of the material. The first indication that this is not the case is the reversibility of the chemical state, as

the sample condition is cycled between UHV and water vapor. As the 2 mbar of water vapor is removed from the sample chamber and the environment is returned to UHV conditions, the sample consistently showed a reversal back to its original state. This indicates that permanent sample damage by X-ray radiation is not occurring. To further exclude the possibility of beam-induced sample damage as a function of X-ray exposure, we performed the following experiment. Sitting at a single point on the sample, we collected four replicate XPS scans under a fixed condition. Following these four scans, the pressure of water vapor was increased from UHV to 0.5 mbar and then to 2.0 mbar. Four replicate scans were collected under each condition. Results of this experiment are shown in Figure S4 in the Supporting Information. If reduction of Fe was the result of X-ray damage, we would expect to observe a steady decrease of Fe³⁺ accompanied by a steady growth of Fe²⁺ as a function of X-ray exposure or scan number. However, instead we observe that the Fe 2p spectrum remains unchanged with the scan number until the water pressure is increased, at which point a stepwise reduction of Fe is observed. These observations indicate that the Fe reduction is a direct result of water exposure and not beam damage due to X-ray irradiation. This measurement also eliminates the possibility that the X-ray irradiation is inducing an electron-transfer-coupled spin transition, which would present as spectral changes as a function of irradiation,⁶⁶ or scan number, rather than the stepwise behavior at each solvation change seen in Figure S4.

A second possibility that could explain the reduction of Fe observed in Figure 5 is photoionization of the gas phase solvent by the X-ray source, followed by electron attachment to Fe. To investigate this possibility, another solvent with a much higher photoionization cross section compared to water, carbon tetrachloride (CCl₄), was introduced to the sample chamber for NAP-XPS measurements. The results from this measurement are shown in Figure S5 of the Supporting Information. In summary, there is a negligible change in either the Fe or Co oxidation states as the sample is transitioned from UHV conditions to exposure to CCl₄ vapor. Fitting these spectra shows that the Fe reduction between UHV and CCl₄ exposure is 11.3%, compared to 83.4% in the case of water. This confirms that X-ray ionization of the background solvent cannot explain the reduction of Fe³⁺ to Fe²⁺ in the presence of water vapor.

Third, having eliminated potential effects of X-ray exposure, we evaluate the possibility of charge transfer between the metal center and a phenanthroline ligand molecule in the Co₃Fe₂ complex. Considering that the aromatic phenanthroline groups may be redox active, it is possible that the electron transfer responsible for Fe reduction comes from a non-innocent phenanthroline ligand. If this is the case, we may expect to observe a shift in the N 1s XPS spectrum corresponding to the oxidation of a phenanthroline ligand. The N 1s spectrum of this complex shows two peaks that can be assigned to the phenanthroline ligands (399 eV) and the cyanide ligands (397 eV), respectively. Figure S8 in the Supporting Information shows the N 1s spectra as a function of temperature and as a function of the chemical environment. In both cases, we observe a minimal shift of the N peaks suggesting that redox activity of the ligands is not responsible for the reduction of Fe observed in Figure 5. To further support this conclusion, we note that the aromatic phenanthroline ligands coordinate only to the equatorial Co centers but that we observe redox

cycling only of the axial Fe centers upon exposure to water vapor.

The fourth mechanism we consider to explain the observed results is that the H-bonding of polar water molecules to the terminal cyanide ligands in the Co_3Fe_2 complex changes the electronic superexchange coupling between Fe and Co. As shown in Figure 1, this can be described as a change in the Robin-Day classification from a strongly coupled complex (class II/III) to a moderately or weakly coupled system (class I). In the presence of water vapor, H-bonding to the terminal cyanide ligands will have an electron-withdrawing effect, which would make the Fe^{3+} centers easier to reduce, resulting in electron transfer from the delocalized system to reduce Fe^{3+} to Fe^{2+} . Because the Fe^{2+} –CN bond length is greater than the Fe^{3+} –CN bond, 1.97 Å vs 1.94 Å in ferro-vs ferricyanide,⁶⁷ this would also reduce the superexchange coupling resulting in a change from a strongly coupled class II/III system to a weakly coupled class I system. In this scenario, we would expect to observe a near unity change in the oxidation state of the axial Fe^{3+} center to Fe^{2+} , while the decoupling of the three equatorial Co centers with the axial Fe would result in a switch from $(\text{Co}^{2.3+})_3$ in the strongly coupled state to $(\text{Co}^{2+})(\text{Co}^{3+})_2$ in the weakly coupled state.

This change, supported by the DFT calculations described above, would be difficult to discern by XPS fitting of the Co 2p spectrum, which simplistically assumes a linear combination of distinct oxidation states and is insufficient to describe a switch from a strongly coupled class II/III system to a weakly coupled class I system. If correct, this mechanism would further imply a change in both the symmetry and the local dipole moment along the equatorial axis of this molecule, whereas in the strongly coupled state all three Co centers are equivalent such that no dipole moment exists in the equatorial plane, while in the weakly coupled system, discrete Co oxidation states would create a significant in-plane dipole moment. Below, we utilize nonlinear, second order sum frequency generation vibrational spectroscopy of the cyanide bands to provide evidence in support of this mechanism.

Chemical Environment-Dependent Vibrational Spectroscopy. For vibrational spectroscopy measurements, the sample was placed in a small enclosed cell filled with either inert argon gas (simulating the anhydrous UHV conditions in Figure 5) or water vapor. While actively purging the cell with either argon or water, a Raman microscope collected vibrational spectra to probe the effect of the chemical environment using the vibrational resonances of the cyanide ligands (2000 – 2200 cm^{-1}) as a reporter. Figure 6A shows that cycling between argon and water results in reversible spectral changes, suggesting that the Raman spectra are sensitive to the same chemically induced switching process as observed above by NAP-XPS measurements. This is not surprising given the important role of the cyanide ligands to control the strength of superexchange coupling between Fe and Co centers.

In the initial spectrum acquired in water vapor (purple, bottom), we observe two features at 2094 and 2133 cm^{-1} , consistent with the nitrile stretch for the terminal and bridging cyanide ligands, respectively. These assignments have been well-reported for Fe- and Co-coordinated cyanide ligands, where terminal Fe–CN ligands display vibrational resonances between 2060 and 2110 cm^{-1} and bridging Fe–CN–Co ligands display resonances from 2090 to greater than 2170 cm^{-1} .^{68–70} Within this range of frequencies, small shifts may reflect changes in the oxidation state of the coordinated metal

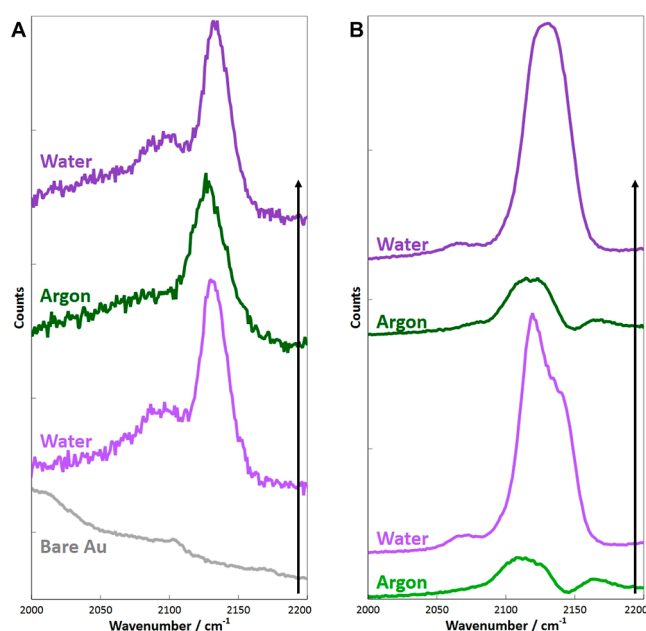


Figure 6. (A) Raman results from one sample exposed in series to water followed by argon and repeated water conditions. Bare Au measurement from the substrate of the sample is shown below in gray, which was subtracted from the other conditions to give absolute sample signal. (B) SFG-VS results from one sample exposed in series to argon and water followed by repeated argon and water conditions.

center, where, in general, reduction of the metal leads to a spectral red shift, while oxidation of the metal leads to a blue shift. These shifts tend to be more sensitive to changes in the Co rather than Fe oxidation state due to the greater σ bonding character of the lower energy N lone pair mixing with the Co in the Co–N bond.⁷⁰

Under initial water conditions, the bridging cyanide peak is centered at 2133 cm^{-1} while the terminal cyanide peak is centered at 2094 cm^{-1} . As argon flows through the cell and water vapor is removed, the bridging cyanide peak red shifts slightly to 2126 cm^{-1} and the terminal cyanide peak broadens (green, middle). Close inspection of the spectrum reveals that the primary peak at 2126 cm^{-1} broadens relative to the spectrum in water with a tail on the low frequency side. Because the spectrum in argon shows only one primary peak with a larger width and a tail at low frequency, we hypothesize that the terminal cyanide stretches, which appeared as a single peak in water having two divalent Fe^{2+} centers, splits in argon where the complex has both an Fe^{2+} and Fe^{3+} center on each apex (see Figure 5). In this state, the blue-shifted terminal cyanide stretches associated with the Fe^{3+} center overlap with the red-shifted bridging cyanide stretches associated with the reduced Co centers. Importantly, these spectral changes are reversible, and reintroduction of water results in nearly exact recovery of the original spectrum (purple, top). These observations are qualitatively consistent with the spectral changes anticipated for an MMCT transition between Fe and Co in the presence and absence of water as a H-bonding solvent.

While the Raman measurements support the assignment of an MMCT driven by a change in chemical environment, it does not specifically resolve the degree of electronic (de)-localization or differentiate between the strongly coupled (Robin-Day class II/III) and weakly coupled (Robin-Day class

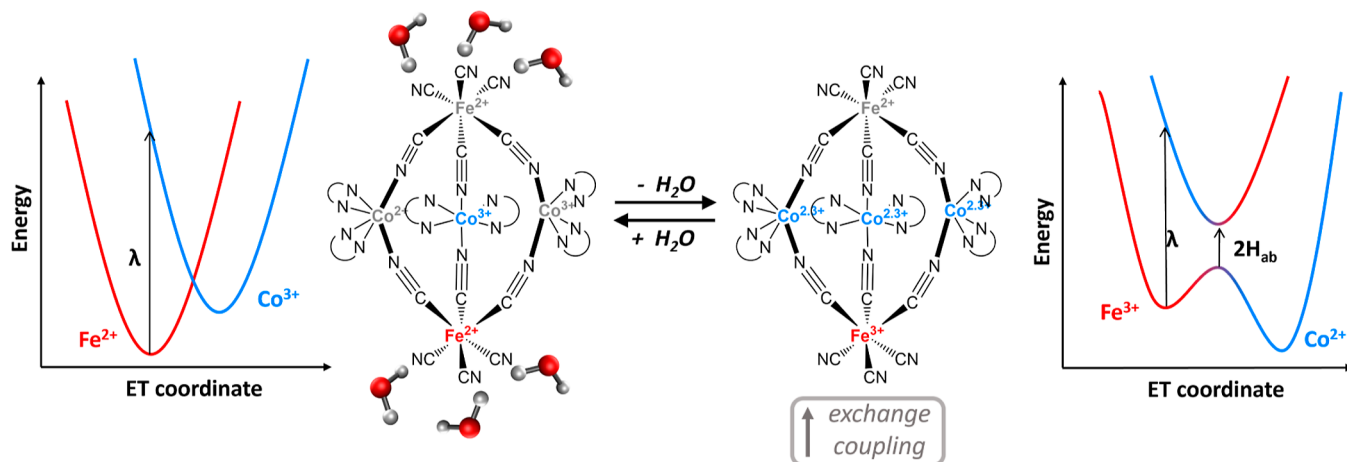


Figure 7. Mechanism for complex changes under ambient and vacuum/argon conditions. There is an MMCT event coupled with a change in the electronic (de)localization, depicted with distinct versus equivalent oxidation states. On the left, the molecule has H-bonding water molecules at the terminal cyanide ligands, reducing the coupling and resulting in a class I system. On the right, exchange coupling increases upon dehydration and the system behaves as a class II/III molecule with indistinguishable Co oxidation states and the absence of an equatorial dipole.

I) pictures. To investigate this question further, we compare the environment-dependent Raman spectra with SFG-VS spectra obtained under identical conditions of argon and water vapor (see Figure 6B). This measurement is insightful because as a second order, nonlinear process, SFG is sensitive to the centrosymmetry of the system, and vibrational resonances become dipole-forbidden in a locally centrosymmetric environment. This indicates that in a strongly coupled state of the molecule where the oxidation states of the three Co centers are identical (see Figure 1B), there should be little or no signal from the bridging cyanide ligands due to the local symmetry of these ligands in the equatorial plane of the molecule.

We note that broken inversion symmetry can also result from non-identical Fe centers on the axial positions of the complex. However, as discussed above, the cyanide stretch of bridging ligands is relatively insensitive to the Fe oxidation state compared to Co oxidation state due to greater σ bonding character of the lower energy N lone pair mixing with the Co. Consequently, we expect the intensity of the bridging Fe–CN–Co stretches to report most sensitively on the molecular symmetry of the equatorial plane as determined by the oxidation states of the Co centers. In this way, SFG intensity becomes a probe of electronic superexchange coupling, where distinct Co oxidation states in a weakly coupled system will show higher signal intensity compared to identical Co oxidation states in a strongly coupled system, which will show little to no SFG intensity.

Figure 6B shows the SFG-VS measurement of a sample cycled between argon and water conditions. The peak shifts between the water and argon environments are the same as the changes observed in the Raman measurements. Exposed to initial argon conditions, the bridging cyanide peak is centered at 2114 cm^{-1} with a broad fwhm indicating that the terminal cyanide peak is spectrally overlapping with the bridging feature. When water is introduced to the sample, the bridging cyanide peak shifts to a central position of 2129 cm^{-1} , while the terminal cyanide peak is isolated at 2069 cm^{-1} . With repeated exposure to argon and water conditions, these features shift reversibly. While the absolute positions and magnitude of the shift are not identical between Figure 6A and B, the qualitative trends match.

Beyond the peak shifts observed in Raman, the SFG results in Figure 6B also display a significant intensity difference depending on the sample environment. In the presence of water, the signal intensity shows approximately a four-fold increase relative to argon. Because SFG is sensitive to the molecular symmetry through the second order polarizability, this observation indicates that the dipole of the molecule changes in the presence or absence of water vapor.

At first, it is surprising that the intensity increases in water and decreases in argon because NAP-XPS measurements show that in water, both Fe centers are in the 2+ oxidation state, while in UHV or argon, the two Fe centers are in different 2+ and 3+ oxidation states. This would suggest that molecular symmetry should increase in water, leading to a loss of the SFG signal. Instead, we see a significant signal enhancement in the presence of water. However, it is important to note that this intensity increase occurs in the bridging rather than the terminal cyanide stretches. This strongly suggests that the spectrum is more sensitive to change in the Co charge states compared with Fe, as expected.

Considering how water vapor can change the charge distribution of the equatorial Co centers, so as to decrease the molecular symmetry and lead to an enhanced SFG signal, we propose the following explanation. In a Robin-Day class II/III system, where electron exchange between Fe and Co is facile, the molecule cannot support distinct oxidation states between Co centers as each is rapidly exchanging electrons with a common Fe center faster than the time scale of a vibrational resonance. In such a scenario, the SFG experiment observes a system in which charge is evenly distributed among the three Co centers, leading to a loss of dipole moment in the equatorial plane of the molecule. Ignoring differences in the oxidation states of the terminal Fe centers, which minimally influence the cyanide stretching frequency, this state of the molecule would render each of the six cyanide ligands degenerate, leading to a high degree of local symmetry. This describes the strongly coupled state of the molecule observed in argon, showing weak SFG intensity of the highly symmetric, six-fold degenerate bridging cyanide stretches.

In contrast, water H-bonds to the terminal cyanide ligands shift charge density to the terminal Fe atoms, leading to reduction of Fe^{3+} to Fe^{2+} by NAP-XPS (see Figure 5). It is

known that a change in Fe oxidation state results in an increase of the Fe–CN bond length,^{67,71} ultimately leading to a decrease in the superexchange coupling because of the reduced orbital overlap and a switch from a Robin-Day class II/III to a class I electronic structure. This reduction in the exchange coupling in the presence of water results in Co centers with discrete oxidation states, which would break the degeneracy of the six bridging cyanide ligands, leading to the formation of an in-plane dipole moment and an observed significant increase in SFG intensity. This mechanism is depicted schematically in Figure 7, which is also consistent with NAP-XPS measurements, which show that the overall charge balance on the Co centers changes between UHV and water vapor (see Figure 4), indicating a change in the charge (de)localization of the system depending on the chemical environment. The vibrational spectroscopy measurements are less sensitive to the electron localization with respect to the Fe centers, and while the NAP-XPS UHV measurements show distinct Fe³⁺ and Fe²⁺ character, this does not exclude the possibility of electron delocalization across the terminal Fe sites on a time scale slower than the coherence time of the XPS probe. However, the mechanism in Figure 7 depicts an asymmetrical superexchange coupling between Co centers and each of the two terminal Fe sites, which is a possibility supported by the distinct Fe XPS signatures. Further investigation of time-resolved electron fluctuation would reveal the nature of total electron localization across each metal center.

Lastly, we confirm that both the changes observed by NAP-XPS and SFG are sensitive to the H-bonding ability of the gas environment. Figure 8A shows the NAP-XPS spectra and Figure 8B shows the SFG spectra of the Co₃Fe₂ complex in UHV or argon, water, and methanol vapor. We observe that the changes in the Fe oxidation state from 3+ to 2+ observed by NAP-XPS are correlated with the intensity of the bridging cyanide ligands observed by SFG and appear to track the H-bonding capacity of the chemical environment. These features steadily increase from the inert environment (UHV or argon) to methanol to water.

CONCLUSIONS

This study compares the effects of temperature and the gas environment on the chemical states of a bistable Co₃Fe₂ complex. Using NAP-XPS as a probe of element-specific oxidation states on Co and Fe centers provides a detailed picture of environment-induced MMCT transitions in this complex. Temperature-dependent NAP-XPS shows an MMCT from Fe to Co, as the temperature is increased from 150 to 375 K. However, NAP-XPS results show that the transition observed when cycling between UHV and water vapor cannot be simply explained as an MMCT transition. Complementary measurements by Raman and SFG-VS reveal that in addition to a chemically induced MMCT, H-bonding of the Co₃Fe₂ complex with water also modulates the strength of superexchange coupling, resulting in a switch from a delocalized to a localized electronic state, involving a corresponding change in the local symmetry and dipole moment of the complex. Specifically, the introduction of H-bonding solvents decreases the strength of superexchange coupling of the Fe–CN–Co system, resulting in a change from a delocalized electronic configuration (Robin-Day class II/III) to a localized electronic configuration (class I) that supports discrete Co center oxidation states, which reduces the molecular symmetry. This change in Robin-Day classification as a function of chemical

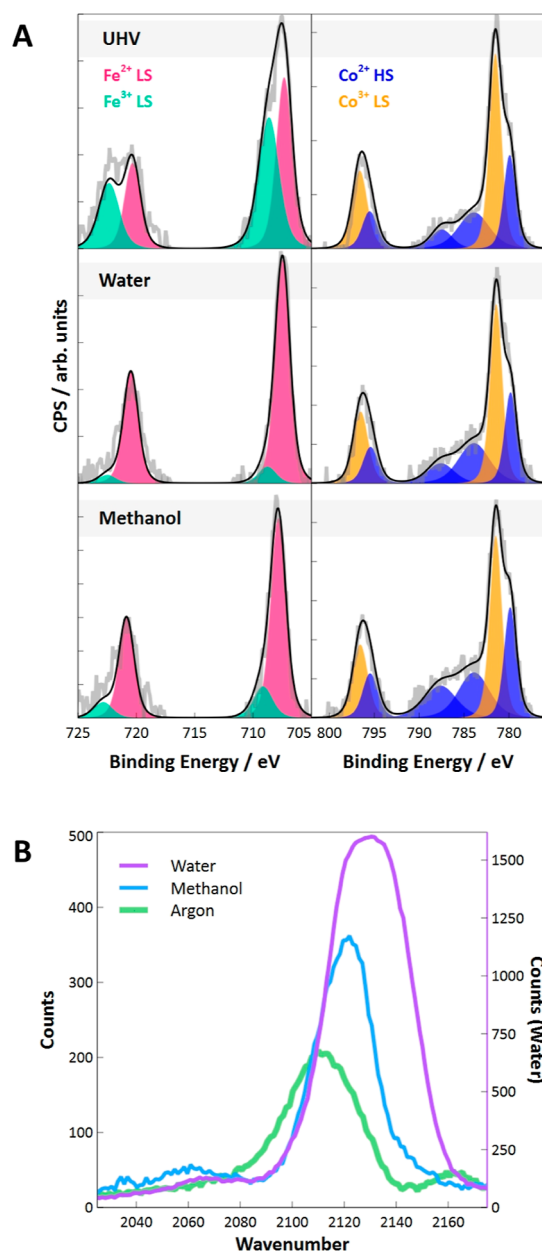


Figure 8. (A) NAP-XPS results under UHV, water, and methanol conditions for the Fe 2p (left) and Co 2p (right) core levels. Total background-subtracted counts are shown as the gray solid line. The total fit is shown as the black solid line. Individual components are highlighted in pink (Fe²⁺), green (Fe³⁺), blue (Co²⁺), and orange (Co³⁺). (B) SFG-VS results from water, methanol, and argon conditions overlaid. The methanol and argon are plotted with absolute counts on the left axis, while water is plotted with absolute counts on the right axis for scaling visual purposes.

environment results in reversible switching of the dipole moment, drawing an analogy to molecular multiferroics having a strong coupling between the local dipole changes and the spin state of the complex, although this molecule cannot be classified as a true molecular multiferroic due to the absence of long-range ordering. These results illustrate the important role of the chemical environment and solvation in the underlying charge and spin transitions in this and related complexes.

■ ASSOCIATED CONTENT

SI Supporting Information

The Supporting Information is available free of charge at <https://pubs.acs.org/doi/10.1021/jacs.3c11451>.

Sample preparation (materials, $[\text{Co}(\text{tmphen})_2]_3[\text{Fe}(\text{CN})_6]_2$ (Co_3Fe_2), Co_3Fe_2 characterization, Co_3Fe_2 solution, solution drop-casting), XPS fitting parameters, NAP-XPS controls (conditional exposure, X-ray exposure, solvent photoionization, CO exposure, N 1s solvent exposure, and C 1s solvent exposure), SFG controls (clean substrate baseline, time delay interference, and sample pseudohomogeneity), single-crystal X-ray structure, and DFT-optimized structures (PDF)

■ AUTHOR INFORMATION

Corresponding Author

L. Robert Baker – Department of Chemistry and Biochemistry, The Ohio State University, Columbus, Ohio 43210, United States; orcid.org/0000-0001-6740-864X; Email: baker.2364@osu.edu

Authors

Emily Hruska – Department of Chemistry and Biochemistry, The Ohio State University, Columbus, Ohio 43210, United States; orcid.org/0000-0002-3558-4937

Quansong Zhu – Department of Chemistry and Biochemistry, The Ohio State University, Columbus, Ohio 43210, United States; orcid.org/0000-0002-5376-1247

Somnath Biswas – Department of Chemistry and Biochemistry, The Ohio State University, Columbus, Ohio 43210, United States; orcid.org/0000-0002-5931-4966

Matthew T. Fortunato – Department of Chemistry and Biochemistry, The Ohio State University, Columbus, Ohio 43210, United States

Dustin R. Broderick – Department of Chemistry and Biochemistry, The Ohio State University, Columbus, Ohio 43210, United States

Christine M. Morales – Department of Chemistry, University of Mount Union, Alliance, Ohio 44601, United States; orcid.org/0000-0001-5813-7219

John M. Herbert – Department of Chemistry and Biochemistry, The Ohio State University, Columbus, Ohio 43210, United States; orcid.org/0000-0002-1663-2278

Claudia Turro – Department of Chemistry and Biochemistry, The Ohio State University, Columbus, Ohio 43210, United States; orcid.org/0000-0003-3202-5870

Complete contact information is available at: <https://pubs.acs.org/doi/10.1021/jacs.3c11451>

Notes

The authors declare the following competing financial interest(s): J.M.H. serves on the board of directors of Q-Chem Inc.

■ ACKNOWLEDGMENTS

This work was primarily supported by Chemical Sciences, Geosciences and Biosciences Division, Office of Basic Energy Sciences, Office of Science, U.S. Department of Energy under DOE Grant no. DE-SC0020977. Synthesis and characterization of the compound were supported by Chemical Sciences, Geosciences and Biosciences Division, Office of Basic Energy Sciences, Office of Science, U.S. Department of

Energy under DOE Grant no. DE-SC0020243. DFT calculations were supported by the National Science Foundation under NSF Grant no. CHE-1955282 and were performed at the Ohio Supercomputer Center.⁷² XPS and NAP-XPS was performed at The Ohio State University Surface Analysis Laboratory. X-ray crystallography was performed at The Ohio State University X-ray Crystallography Laboratory. We thank Dr. Yehia Khalifa and Melissa Marx for assistance with NAP-XPS measurements, Dr. Curtis Moore for assistance with X-ray crystallography measurements, and Prof. Zachary Schultz and Dr. Chelsea Zoltowski for assistance with Raman measurements.

■ REFERENCES

- (1) Wasielewski, M. R.; Forbes, M. D.; Frank, N. L.; Kowalski, K.; Scholes, G. D.; Yuen-Zhou, J.; Baldo, M. A.; Freedman, D. E.; Goldsmith, R. H.; Goodson, T.; et al. Exploiting chemistry and molecular systems for quantum information science. *Nat. Rev. Chem.* **2020**, *4*, 490–504.
- (2) Gaita-Ariño, A.; Luis, F.; Hill, S.; Coronado, E. Molecular spins for quantum computation. *Nat. Chem.* **2019**, *11*, 301–309.
- (3) Stajic, J. The future of quantum information processing. *Science* **2013**, *339*, 1163.
- (4) Ardavan, A.; Rival, O.; Morton, J. J.; Blundell, S. J.; Tyryshkin, A. M.; Timco, G. A.; Winpenny, R. E. Will spin-relaxation times in molecular magnets permit quantum information processing? *Phys. Rev. Lett.* **2007**, *98*, 057201.
- (5) Hamlin, J. J.; Zhou, B. B. Extreme diamond-based quantum sensors. *Science* **2019**, *366*, 1312–1313.
- (6) Carmeli, I.; Kumar, K. S.; Heifler, O.; Carmeli, C.; Naaman, R. Spin selectivity in electron transfer in photosystem I. *Angew. Chem., Int. Ed.* **2014**, *53*, 8953–8958.
- (7) Mai, S.; González, L. Molecular photochemistry: recent developments in theory. *Angew. Chem., Int. Ed.* **2020**, *59*, 16832–16846.
- (8) Lambert, N.; Chen, Y.-N.; Cheng, Y.-C.; Li, C.-M.; Chen, G.-Y.; Nori, F. Quantum biology. *Nat. Phys.* **2013**, *9*, 10–18.
- (9) Pan, L.; Ai, M.; Huang, C.; Yin, L.; Liu, X.; Zhang, R.; Wang, S.; Jiang, Z.; Zhang, X.; Zou, J.-J.; et al. Manipulating spin polarization of titanium dioxide for efficient photocatalysis. *Nat. Commun.* **2020**, *11*, 418.
- (10) Ferlay, S.; Mallah, T.; Ouahes, R.; Veillet, P.; Verdagner, M. A room-temperature organometallic magnet based on Prussian blue. *Nature* **1995**, *378*, 701–703.
- (11) Entley, W. R.; Girolami, G. S. High-temperature molecular magnets based on cyanovanadate building blocks: spontaneous magnetization at 230 K. *Science* **1995**, *268*, 397–400.
- (12) Holmes, S. M.; Girolami, G. S. Sol–Gel Synthesis of $\text{KV}^{\text{II}}[\text{Cr}^{\text{III}}(\text{CN})_6] \cdot 2\text{H}_2\text{O}$: A Crystalline Molecule-Based Magnet with a Magnetic Ordering Temperature above 100 °C. *J. Am. Chem. Soc.* **1999**, *121*, 5593–5594.
- (13) Sato, O.; Iyoda, T.; Fujishima, A.; Hashimoto, K. Photoinduced magnetization of a cobalt-iron cyanide. *Science* **1996**, *272*, 704–705.
- (14) Beauvais, L. G.; Long, J. R. $\text{Co}_3[\text{Co}(\text{CN})_5]_2$: A microporous magnet with an ordering temperature of 38 K. *J. Am. Chem. Soc.* **2002**, *124*, 12096–12097.
- (15) Berlinguette, C. P.; Vaughn, D.; Cañada-Vilalta, C.; Galán-Mascarós, J. R.; Dunbar, K. R. A Trigonal-Bipyramidal Cyanide Cluster with Single-Molecule-Magnet Behavior: Synthesis, Structure, and Magnetic Properties of $\{[\text{Mn}^{\text{II}}(\text{tmphen})_2]_3[\text{Mn}^{\text{III}}(\text{CN})_6]_2\}$. *Angew. Chem., Int. Ed.* **2003**, *42*, 1523–1526.
- (16) Shatruk, M.; Chambers, K. E.; Prosvirin, A. V.; Dunbar, K. R. Systematic investigation of trigonal-bipyramidal cyanide-bridged clusters of the first-row transition metals. *Inorg. Chem.* **2007**, *46*, 5155–5165.
- (17) Shatruk, M.; Dragulescu-Andrasi, A.; Chambers, K. E.; Stoian, S. A.; Bominaar, E. L.; Achim, C.; Dunbar, K. R. Properties of Prussian blue materials manifested in molecular complexes:

observation of cyanide linkage isomerism and spin-crossover behavior in pentanuclear cyanide clusters. *J. Am. Chem. Soc.* **2007**, *129*, 6104–6116.

(18) Berlinguette, C. P.; Dragulescu-Andrasi, A.; Sieber, A.; Galán-Mascarós, J. R.; Güdel, H. U.; Achim, C.; Dunbar, K. R. A Charge-Transfer-Induced Spin Transition in the Discrete Cyanide-Bridged Complex $\{[\text{Co}(\text{tmphen})_2]_3[\text{Fe}(\text{CN})_6]_2\}$. *J. Am. Chem. Soc.* **2004**, *126*, 6222–6223.

(19) Shimamoto, N.; Ohkoshi, S.-i.; Sato, O.; Hashimoto, K. Control of charge-transfer-induced spin transition temperature on cobalt-iron Prussian blue analogues. *Inorg. Chem.* **2002**, *41*, 678–684.

(20) Roman, M. A.; Reu, O. S.; Klokishner, S. I. Charge-transfer-induced spin transitions in crystals containing cyanide-bridged Co-Fe clusters: role of intra- and intercluster interactions. *J. Phys. Chem. A* **2012**, *116*, 9534–9544.

(21) Zimara, J.; Stevens, H.; Oswald, R.; Demeshko, S.; Dechert, S.; Mata, R. A.; Meyer, F.; Schwarzer, D. Time-Resolved Spectroscopy of Photoinduced Electron Transfer in Dinuclear and Tetranuclear Fe/Co Prussian Blue Analogues. *Inorg. Chem.* **2021**, *60*, 449–459.

(22) Schnaubelt, L.; Petzold, H.; Dmitrieva, E.; Rosenkranz, M.; Lang, H. A solvent- and temperature-dependent intramolecular equilibrium of diamagnetic and paramagnetic states in Co complexes bearing triaryl amines. *Dalton Trans.* **2018**, *47*, 13180–13189.

(23) Nadurata, V. L.; Boskovic, C. Switching metal complexes via intramolecular electron transfer: connections with solvatochromism. *Inorg. Chem. Front.* **2021**, *8*, 1840–1864.

(24) Funck, K. E.; Prosvirin, A. V.; Mathonière, C.; Clérac, R.; Dunbar, K. R. Light-induced excited spin state trapping and charge transfer in trigonal bipyramidal cyanide-bridged complexes. *Inorg. Chem.* **2011**, *50*, 2782–2789.

(25) Létard, J. F. Photomagnetism of iron (II) spin crossover complexes—the T (LIESST) approach. *J. Mater. Chem.* **2006**, *16*, 2550–2559.

(26) Bleuzen, A.; Marvaud, V.; Mathoniere, C.; Sieklucka, B.; Verdaguer, M. Photomagnetism in clusters and extended molecule-based magnets. *Inorg. Chem.* **2009**, *48*, 3453–3466.

(27) Manriquez, J. M.; Yee, G. T.; McLean, R. S.; Epstein, A. J.; Miller, J. S. A room-temperature molecular/organic-based magnet. *Science* **1991**, *252*, 1415–1417.

(28) Blundell, S. J.; Pratt, F. L. Organic and molecular magnets. *J. Phys.: Condens. Matter* **2004**, *16*, R771–R828.

(29) Miller, J. S.; Epstein, A. J. Organic and organometallic molecular magnetic materials—designer magnets. *Angew. Chem. Int. Ed. Engl.* **1994**, *33*, 385–415.

(30) Miller, J. S. Magnetically ordered molecule-based materials. *Chem. Soc. Rev.* **2011**, *40*, 3266–3296.

(31) Ungur, L.; Chibotaru, L. F. Strategies toward high-temperature lanthanide-based single-molecule magnets. *Inorg. Chem.* **2016**, *55*, 10043–10056.

(32) Long, J.; Guari, Y.; Ferreira, R. A.; Carlos, L. D.; Larionova, J. Recent advances in luminescent lanthanide based Single-Molecule Magnets. *Coord. Chem. Rev.* **2018**, *363*, 57–70.

(33) Ren, M.; Zheng, L.-M. Lanthanide-based single molecule magnets. *Acta Chim. Sin.* **2015**, *73*, 1091.

(34) Liu, J.-L.; Chen, Y.-C.; Tong, M.-L. Symmetry strategies for high performance lanthanide-based single-molecule magnets. *Chem. Soc. Rev.* **2018**, *47*, 2431–2453.

(35) Benelli, C.; Gatteschi, D. *Introduction to Molecular Magnetism: From Transition Metals to Lanthanides*; John Wiley & Sons, 2015.

(36) Parker, D.; Sutura, E. A.; Kuprov, I.; Chilton, N. F. How the ligand field in lanthanide coordination complexes determines magnetic susceptibility anisotropy, paramagnetic NMR shift, and relaxation behavior. *Acc. Chem. Res.* **2020**, *53*, 1520–1534.

(37) Gomez-Coca, S.; Cremades, E.; Aliaga-Alcalde, N.; Ruiz, E. Mononuclear single-molecule magnets: tailoring the magnetic anisotropy of first-row transition-metal complexes. *J. Am. Chem. Soc.* **2013**, *135*, 7010–7018.

(38) Wang, J.-H.; Li, Z.-Y.; Yamashita, M.; Bu, X.-H. Recent progress on cyano-bridged transition-metal-based single-molecule

magnets and single-chain magnets. *Coord. Chem. Rev.* **2021**, *428*, 213617.

(39) Bar, A. K.; Pichon, C.; Sutter, J.-P. Magnetic anisotropy in two- to eight-coordinated transition-metal complexes: Recent developments in molecular magnetism. *Coord. Chem. Rev.* **2016**, *308*, 346–380.

(40) Dunbar, K. R.; Heintz, R. A.; et al. Chemistry of transition metal cyanide compounds: Modern perspectives. *Prog. Inorg. Chem.* **1996**, *45*, 283–391.

(41) Shatruk, M.; Avendano, C.; Dunbar, K. R. Cyanide-bridged complexes of transition metals: A molecular magnetism perspective. *Prog. Inorg. Chem.* **2009**, *56*, 155–334.

(42) Meng, L.; Deng, Y.-F.; Zhang, Y.-Z. Anion-Dependent Electron Transfer in the Cyanide-Bridged $[\text{Fe}_2\text{Co}_2]$ Capsules. *Inorg. Chem.* **2021**, *60*, 14330–14335.

(43) Han, M. J.; Ozaki, T.; Yu, J. Electronic structure, magnetic interactions, and the role of ligands in Mnⁿ (n = 4, 12) single-molecule magnets. *Phys. Rev. B* **2004**, *70*, 184421.

(44) Sharma, P.; Truhlar, D. G.; Gagliardi, L. Magnetic coupling in a tris-hydroxo-bridged chromium dimer occurs through ligand mediated superexchange in conjunction with through-space coupling. *J. Am. Chem. Soc.* **2020**, *142*, 16644–16650.

(45) Robin, M. B.; Day, P. Mixed valence chemistry—a survey and classification. *Adv. Inorg. Chem. Radiochem.* **1968**, *10*, 247–422.

(46) Demadis, K. D.; Hartshorn, C. M.; Meyer, T. J. The localized-to-delocalized transition in mixed-valence chemistry. *Chem. Rev.* **2001**, *101*, 2655–2686.

(47) Parthey, M.; Kaupp, M. Quantum-chemical insights into mixed-valence systems: within and beyond the Robin–Day scheme. *Chem. Soc. Rev.* **2014**, *43*, 5067–5088.

(48) Funck, K. E.; Hilfiger, M. G.; Berlinguette, C. P.; Shatruk, M.; Wernsdorfer, W.; Dunbar, K. R. Trigonal-bipyramidal metal cyanide complexes: a versatile platform for the systematic assessment of the magnetic properties of Prussian blue materials. *Inorg. Chem.* **2009**, *48*, 3438–3452.

(49) Berlinguette, C. P.; Dragulescu-Andrasi, A.; Sieber, A.; Güdel, H. U.; Achim, C.; Dunbar, K. R. A charge-transfer-induced spin transition in a discrete complex: the role of extrinsic factors in stabilizing three electronic isomeric forms of a cyanide-bridged Co/Fe cluster. *J. Am. Chem. Soc.* **2005**, *127*, 6766–6779.

(50) Wallentine, S.; Bandaranayake, S.; Biswas, S.; Baker, L. R. Plasmon-resonant vibrational sum frequency generation of electrochemical interfaces: Direct observation of carbon dioxide electro-reduction on gold. *J. Phys. Chem. A* **2020**, *124*, 8057–8064.

(51) Zhu, Q.; Wallentine, S. K.; Deng, G.-H.; Rebstock, J. A.; Baker, L. R. The solvation-induced Onsager reaction field rather than the double-layer field controls CO₂ reduction on gold. *JACS Au* **2022**, *2*, 472–482.

(52) Renz, M.; Theilacker, K.; Lambert, C.; Kaupp, M. A reliable quantum-chemical protocol for the characterization of organic mixed-valence compounds. *J. Am. Chem. Soc.* **2009**, *131*, 16292–16302.

(53) Grimme, S.; Antony, J.; Ehrlich, S.; Krieg, H. A consistent and accurate *ab initio* parameterization of density functional dispersion correction (DFT-D) for the 94 elements H–Pu. *J. Chem. Phys.* **2010**, *132*, 154104.

(54) Neese, F. Prediction of molecular properties and molecular spectroscopy with density functional theory: From fundamental theory to exchange-coupling. *Coord. Chem. Rev.* **2009**, *253*, 526–563.

(55) Epifanovsky, E.; Gilbert, A. T. B.; Feng, X.; Lee, J.; Mao, Y.; Mardirossian, N.; Pokhilko, P.; White, A. F.; Coons, M. P.; Dempwolff, A. L.; et al. Software for the frontiers of quantum chemistry: An overview of developments in the Q-Chem 5 package. *J. Chem. Phys.* **2021**, *155*, 084801.

(56) Szilagy, R. K.; Winslow, M. A. On the accuracy of density functional theory for iron–sulfur clusters. *J. Comput. Chem.* **2006**, *27*, 1385–1397.

(57) Ren, F.; Liu, F. Impacts of polarizable continuum models on the SCF convergence and DFT delocalization error of large molecules. *J. Chem. Phys.* **2022**, *157*, 184106.

(58) Bowling, P. E.; Broderick, D. R.; Herbert, J. M. Fragment-based calculations of enzymatic thermochemistry require dielectric boundary conditions. *J. Phys. Chem. Lett.* **2023**, *14*, 3826–3834.

(59) Lange, A. W.; Herbert, J. M. Polarizable continuum reaction-field solvation models affording smooth potential energy surfaces. *J. Phys. Chem. Lett.* **2010**, *1*, 556–561.

(60) Lange, A. W.; Herbert, J. M. A smooth, nonsingular, and faithful discretization scheme for polarizable continuum models: The switching/Gaussian approach. *J. Chem. Phys.* **2010**, *133*, 244111.

(61) Herbert, J. M. Dielectric continuum methods for quantum chemistry. *Wiley Interdiscip. Rev.: Comput. Mol. Sci.* **2021**, *11*, No. e1519.

(62) Kaichev, V. V.; Saraev, A. A.; Matveev, A. V.; Dubinin, Y. V.; Knop-Gericke, A.; Bukhtiyarov, V. I. In situ NAP-XPS and mass spectrometry study of the oxidation of propylene over palladium. *J. Phys. Chem. C* **2018**, *122*, 4315–4323.

(63) Nguyen, L.; Tao, F. F.; Tang, Y.; Dou, J.; Bao, X.-J. Understanding catalyst surfaces during catalysis through near ambient pressure X-ray photoelectron spectroscopy. *Chem. Rev.* **2019**, *119*, 6822–6905.

(64) Zhong, L.; Chen, D.; Zafeiratos, S. A mini review of in situ near-ambient pressure XPS studies on non-noble, late transition metal catalysts. *Catal. Sci. Technol.* **2019**, *9*, 3851–3867.

(65) Toyoshima, R.; Kondoh, H. In-situ observations of catalytic surface reactions with soft x-rays under working conditions. *J. Phys.: Condens. Matter* **2015**, *27*, 083003.

(66) Sekine, Y.; Nihei, M.; Kumai, R.; Nakao, H.; Murakami, Y.; Oshio, H. X-ray-induced phase transitions by selective excitation of heterometal ions in a cyanide-bridged Fe–Co molecular square. *Chem. Commun.* **2014**, *50*, 4050–4052.

(67) Smith, D. A.; Heeg, M.; Heineman, W. R.; Elder, R. Direct determination of Fe–C bond lengths in iron (II) and iron (III) cyanide solutions using EXAFS spectroelectrochemistry. *J. Am. Chem. Soc.* **1984**, *106*, 3053–3054.

(68) Hester, R. E.; Nour, E. M. Resonance-Raman and infrared studies of cyanide-bridged dimetal complexes. *J. Chem. Soc., Dalton Trans.* **1981**, 939–941.

(69) Nihei, M.; Sekine, Y.; Suganami, N.; Nakazawa, K.; Nakao, A.; Nakao, H.; Murakami, Y.; Oshio, H. Controlled intramolecular electron transfers in cyanide-bridged molecular squares by chemical modifications and external stimuli. *J. Am. Chem. Soc.* **2011**, *133*, 3592–3600.

(70) Kettle, S. F.; Diana, E.; Boccaleri, E.; Stanghellini, P. L. The vibrational spectra of the cyanide ligand revisited. Bridging cyanides. *Inorg. Chem.* **2007**, *46*, 2409–2416.

(71) Nihei, M.; Yanai, Y.; Hsu, I.-J.; Sekine, Y.; Oshio, H. A Hydrogen-Bonded Cyanide-Bridged [Co₂Fe₂] Square Complex Exhibiting a Three-Step Spin Transition. *Angew. Chem., Int. Ed.* **2017**, *56*, 591–594.

(72) Ohio Supercomputer Center. <http://osc.edu/ark:/19495/f5s1ph73> (accessed Jan 10, 2024).